

We are IntechOpen, the world's leading publisher of Open Access books Built by scientists, for scientists

6,900

Open access books available

186,000

International authors and editors

200M

Downloads

Our authors are among the

154

Countries delivered to

TOP 1%

most cited scientists

12.2%

Contributors from top 500 universities



WEB OF SCIENCE™

Selection of our books indexed in the Book Citation Index
in Web of Science™ Core Collection (BKCI)

Interested in publishing with us?
Contact book.department@intechopen.com

Numbers displayed above are based on latest data collected.
For more information visit www.intechopen.com



Optoelectronic Design of a Closed-Loop Depolarized IFOG with Sinusoidal Phase Modulation for Intermediate Grade Applications

Ramón José Pérez Menéndez

Additional information is available at the end of the chapter

<http://dx.doi.org/10.5772/intechopen.72592>

Abstract

A depolarized fiber optic gyroscope (DFOG) prototype with closed-loop configuration, sinusoidal-bias, and serrodyne-feedback electrooptic phase modulations was designed. A complete optoelectronic design is realized by using computational simulation tools (optical subsystem: Synopsys[®]-Optsim[™] software and electronic subsystem: National Instruments[®]-MultiSim[™] software). The design presented here includes both optical and electronic circuits, being the main innovation, is the use of an analogical integrator provided with reset and placed in the feedback of the electrooptic phase-modulation chain that produces a serrodyne-shaped voltage ramp signal for obtaining the interferometric signal phase cancellation. The performance obtained for this model (threshold sensitivity $\leq 0.052^\circ/\text{h}$; dynamic range = $\pm 78.19^\circ/\text{s}$) does reach the IFOG intermediate grade (tactical and industrial applications) and does demonstrate the suitability and reliability of simulation-based software tools for this kind of optoelectronic design.

Keywords: interferometric-fiber-optic-gyroscope (IFOG), depolarized-fiber-optic-gyroscope (DFOG), super-luminescent-laser-diode (SLD), single-mode-fiber (SMF), phase-modulator (PM), closed-loop configuration, bias phase-modulation, feedback phase-modulation, serrodyne-wave, IFOG intermediate grade, IFOG navigation grade, phase-sensitive-demodulator (PSD), Lyot depolarizer

1. Introduction

In all the electro-optical engineering areas, particularly in the design of high-cost devices like IFOGs, the computational simulation resources can provide a powerful and inestimable advance. It stems from the rapidity, the reproducibility, and the reliability of this kind of hardware to obtain the ultimate design of a preconceived model. Furthermore, it is possible to obtain substantial cost savings in components and time consuming for the model assembly in optical bench. Only after having obtained an ideal design so much for the performance characteristics all that for the adaptation to a specific application, it is suitable to initiate the laboratory manufacture stage for the prototype designed previously. In this article, it is shown to the reader an aspect that is not usually in the literature, namely: how to realize the simulation of a classical IFOG system without having to make the real model in the laboratory. For this proposal, three classical electrooptic simulation tools: Synopsys™ OptSim®, National Instruments™ MultiSim® and MathWorks™ Matlab-Simulink® will be used. In the present decade, the design trends on interferometric fiber optic gyroscope (IFOG) are focused on devices with very high performance (navigation-grade, sensitivity $\leq 0.001^\circ/\text{h}$), mainly targeting aeronautics and spacecraft applications. Nevertheless, it is also possible to realize designs for certain applications that do not need such a high grade of performance (intermediate-grade, sensitivity $\leq 0.01^\circ/\text{h}$ or industrial-grade, sensitivity $\leq 1^\circ/\text{h}$). The latter mentioned will constitute the objective of the model presented. What continues next is a brief overview of the basis of IFOG performance.

The nonreciprocal phase shift between the two waves in counter-propagation (clockwise and counterclockwise) induced by rotation when both propagate across the sensing coil of optical-fiber, also known as Sagnac effect, is usually given by the expression (see, for instance, [1–10]):

$$\phi_s = \frac{2\pi L D}{\lambda c} \Omega \quad (1)$$

being L the total length (m) of the sensing coil, D its diameter (m), Ω the rotation rate (rad/s), and ϕ_s is the phase shift difference (rad), λ and c are the wavelength (m) and the speed of light (m/s) in free space, respectively, of the radiation emitted by the laser source. The proportionality factor that precedes the rotation-ratio is known as the scale-factor (SF) of the gyroscope, and it is a basic constructive constant that depends on geometric and optical parameters of the device. Taking the following initial values for the design: $L = 300$ m, $D = 0.08$ m, and $\lambda = 1310$ nm, a value of $1.86 \mu\text{rad}/(^\circ/\text{h})$ is obtained for SF. A detailed study of the depolarization mechanism of optical counter-propagated waves within the fiber optic sensing coil can be consulted in [11–17]. The main advantage of the depolarization technique is that this approach allows using a single-mode optical fiber for the sensing coil, with the consequent economic savings on optical components costs of the gyroscope. This design is based on a conventional IFOG structure (interferometric fiber optic gyroscope) with a sinusoidal electrooptic phase modulation and a closed-loop feedback phase modulation realized with classic analogical electronic components, which provides a better stability and linearity of the gyroscope's SF, while using cost-competitive components. The rest of the paper is organized as follows. The next section (Section 2) is focused on the design of optical and electronic sub-systems of the model. Section 3 provides some important calculations and estimations of the performance of the design, and Section 4 shows

the simulation results (optical and electronic subsystems). Finally, Section 5 includes a discussion on simulation results, and Section 6 collects the main conclusions of this paper.

2. Sensor design

2.1. Design of the optical system

The components of the optical system of this gyroscope are depicted in **Figure 1**. The light source is a 1310 nm superluminescent diode (SLD) with a Gaussian low ripple spectral profile. For this unit, the commercial reference SLD1024S of Thorlabs was used, with DIL-14 pin assembly package, with FC/APC fiber pigtailed and realized in standard single-mode optical fiber. This unit provides an adjustable optical power up to 22 mW maximum level, although only 5 mW maximum level is needed for the present model. This unit takes an integrated thermistor to perform the temperature control, so that it is possible to obtain the stabilization of the power source on the spectral range. Accordingly with the temperature stabilization, the chip package must not exceed a maximum temperature of 65°C. The directional optical coupler is four ports (2×2 configuration), with 50/50 output ratio, realized with fiber-optic side-polished technique, and an insertion loss of 0.60 dB. The linear polarizer placed at the output of the directional input-output coupler is featured in polarization-maintaining fiber (PMF) with a 2.50 m length, insertion loss of 0.1dB, and a polarization extinction ratio (PER) > 50 dB. The integrated optical circuit IOC (integrated optical chip) performs the function of optical directional coupler at the input of the sensing fiber-optic coil (Y-Junction) and also the function of electro-optic phase modulator (PM). In a more advanced design, the linear fiber-optic polarizer

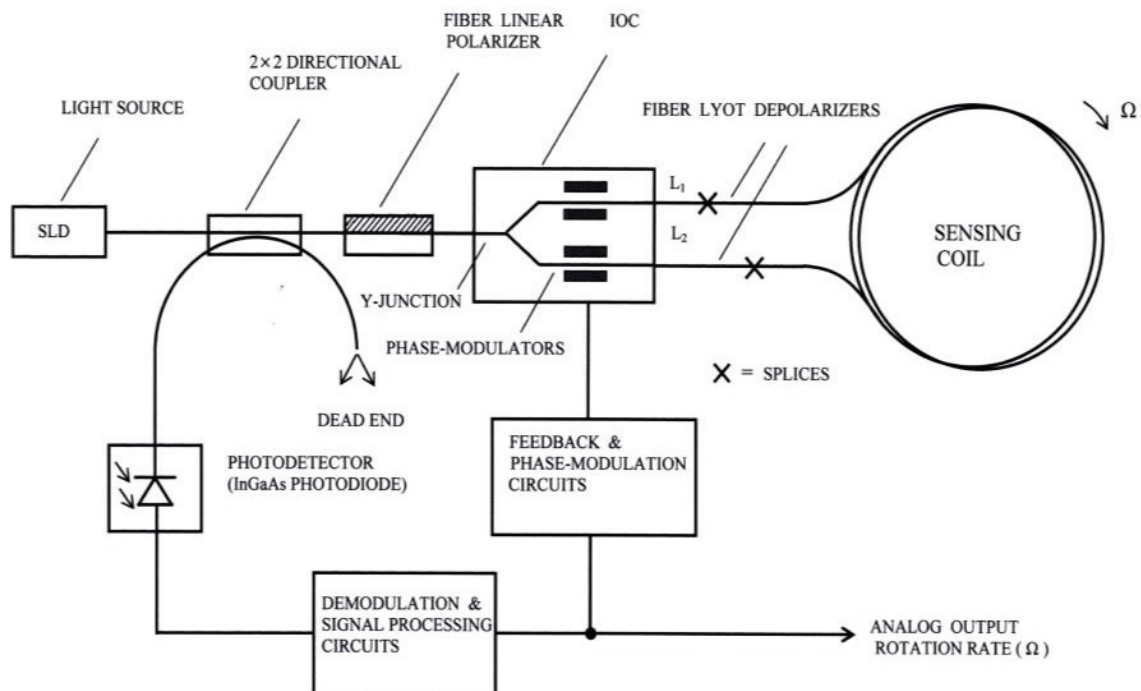


Figure 1. Electro-optical system configuration.

can be replaced by an integrated approach, so that the former remains joined at the input of the IOC wave-guide [18]. This way, the bulk optic polarizer is avoided, which is one important contribution to reduce the whole space occupied by the optical system of the gyroscope.

The chosen PM is electro-optical class. Its electrodes remain parallel to the wave-guide channels obtained by diffusion of Ti on a lithium-niobate (LiNbO₃) substrate. The PM zone of the IOC includes two pairs of electrodes placed symmetrically with regard to the central axis of the integrated block. The output ports of the IOC remain connected, respectively, to the heads of the two Lyot depolarizers (both made on PM-fiber), with lengths L₁ and L₂, respectively. These Lyot depolarizers are realized in polarization-maintaining optical fiber (PMF), connecting two segments appropriate lengths, so that the axes of birefringence of both form angles of 45°.

Calculations of Lyot depolarizer lengths are shown next. Calculated lengths L₁ and L₂ of the Lyot depolarizers summarize 26.20 and 52.40 cm, respectively.

‘cálculo despolarizadores Lyot

$$\frac{L_D}{L_c} \cong \frac{L_b}{\lambda} \Rightarrow L_D \cong \frac{L_c L_b}{\lambda} \approx \frac{(20\lambda) \left(\frac{\lambda}{B}\right)}{\lambda} = \frac{(20\lambda) \left(\frac{\lambda}{|n_X - n_Y|}\right)}{\lambda}$$

$$L_c \approx 20\lambda = 20 \times (1310 \times 10^{-9}) = 26.20 \times 10^{-6} [m] = 26.20 [\mu m] \quad (= \text{coherence source length})$$

$$L_b = \frac{\lambda}{|n_X - n_Y|} = \frac{1310 \times 10^{-9}}{1 \times 10^{-4}} = 10000 \times (1310 \times 10^{-9}) = 1.310 \times 10^{-2} [m]$$

(= fiber-optical beat length)

$$L_D \cong \frac{(26.20 \times 10^{-6})(1.310 \times 10^{-2})}{1310 \times 10^{-9}} = 26.20 \times 10^{-2} [m] (= \text{fiber-optical depolarization length})$$

$$L_1 = L_D = 26.20 [cm]$$

$$L_2 = 2L_1 = 2 \times 26.20 [cm] = 52.40 [cm]$$

$$\theta = 45^\circ \quad (= \text{angle between main birefringence axis of two fibers at splices})$$

These calculations were realized taking into account a 26.20 μm value for the coherence length of a broadband light source (emitting at 1310 nm wavelength) and a 13.10 mm value for the beat length of optical fiber. The two optical waves CW (clockwise) and CCW (counterclockwise) coming from the sensing coil gather together on the Y-Junction placed at the input of the IOC. The sensing coil consists of 300 m of optical standard single-mode fiber (commercial type SMF28), made by quadrupolar winding on a spool of 8 cm average-diameter, which provides 1194 turns. This optical fiber presents the following structural characteristics: step refractive index, basis material = fused-silica, external coating = acrylate, core diameter = 8.2 μm, cladding diameter = 125 ± 0.7 μm, and external coating diameter = 245 ± 5 μm, with the following optical parameters: n_{core} = 1.467, n_{cladding} = 1.460, NA = 0.143, maximum attenuation = 0.35 dB/km at 1310 nm, h-parameter = 2 × 10⁻⁶ m⁻¹, dispersion coefficient ≤ 18.0 ps/(nm × km) at 1550 nm, polarization dispersion coefficient ≤ 0.2 ps/km^{1/2}, birefringence: B = 1.0 × 10⁻⁶.

The chosen PM is electro-optical class. Its electrodes remain parallel to the wave-guide channels obtained by diffusion of Ti on a lithium-niobate (LiNbO₃) substrate. The PM zone of the

IOC includes two pairs of electrodes placed symmetrically with regard to the central axis of the integrated block. The output ports of the IOC remain connected, respectively, to the heads of the two Lyot depolarizers (both made on PM-fiber), with lengths L_1 and L_2 , respectively. These Lyot depolarizers are realized in polarization-maintaining optical fiber (PMF), connecting two segments of appropriate lengths, so that the axes of birefringence of both form angles of 45° .

2.2. Design of the electronic system

In absence of rotation ($\Omega = 0$ rad/s), the transit-time of the two counter-propagated waves across the sensing coil is τ seconds, being its value:

$$\tau = \frac{L}{\left(\frac{c}{n_{core}}\right)} = \frac{n_{core} L}{c} \quad (2)$$

With the values of parameters adopted previously for the model design, assuming 1467 for n_{core} value and using 1194 turns of optical-fiber wrapped on standard fiber-optic coil, the resultant value for the transit time is $\tau = 1.467 \mu\text{s}$. On the other hand, the transit time value also determines the value of modulation frequency f_m that must be applied to Phase-Modulator (PM), given by the expression:

$$f_m = \frac{1}{2\tau} \quad (3)$$

resulting, for the present design in a calculated value of 340.83 kHz. Equation (3) comes from the condition of maximum amplitude of the bias phase-difference modulation for the optical wave, which is possible to formulate by the following expression:

$$\Delta\phi_{bias}(t) = 2\phi_0 \sin\left(\frac{2\pi f_m \tau}{2}\right) \cos\left[2\pi f_m \left(t - \frac{\tau}{2}\right)\right] \quad (4)$$

The condition of maximum amplitude needs the $2\pi f_m \tau = \pi$ relation to be satisfied (and then, Eq. (3) is accomplished). The block diagram of the electronic scheme for phase modulation and demodulation circuits is represented in **Figure 2**. A closed-loop configuration has been adopted with sinusoidal bias phase modulation and serrodyne feedback phase modulation, taking as initial reference the state-of-the-art of demodulation circuits reported till now [19–24].

However, and this is the novelty, it has been changed the structure of feedback chain, adding now a new design of analogical integrator which incorporates one FET transistor (2N3848) as it is depicted in **Figure 3**. The function of this transistor is realizing periodically the shortcut of the capacitor therefore nulling instantaneously the voltage on feedback branch of integrator OPAMP. The time period for shortcut FET transistor is driving by the value of V_{gate} voltage, which, in turn, is controlled by an unstable Flip-Flop circuit.

Referring to **Figure 3**, block #7 generates a linear ramp voltage V_γ on its output, and this ramp resets each time period driving by V_{gate} voltage. In this way, a resultant serrodyne-wave voltage is easily generated at the output of this integrator circuit, obtaining finally the same

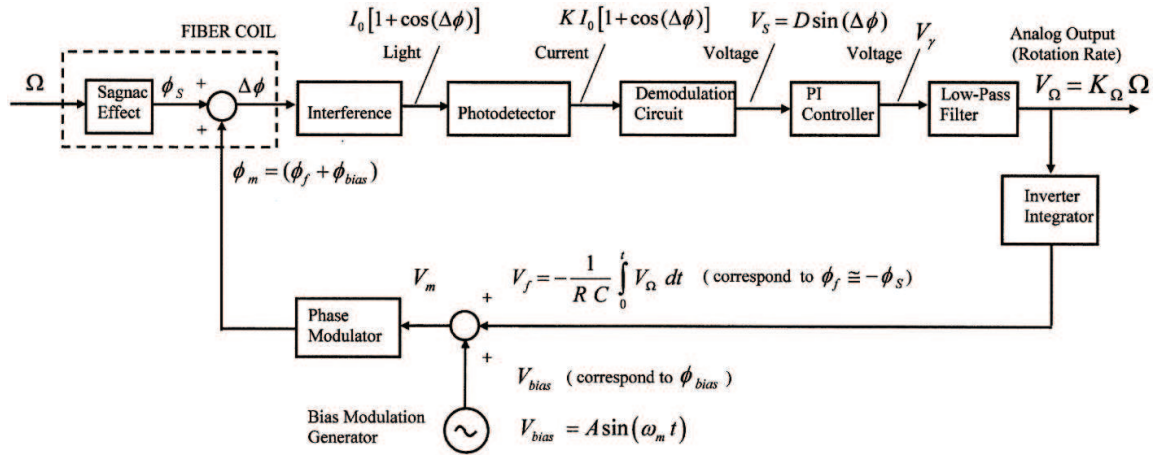


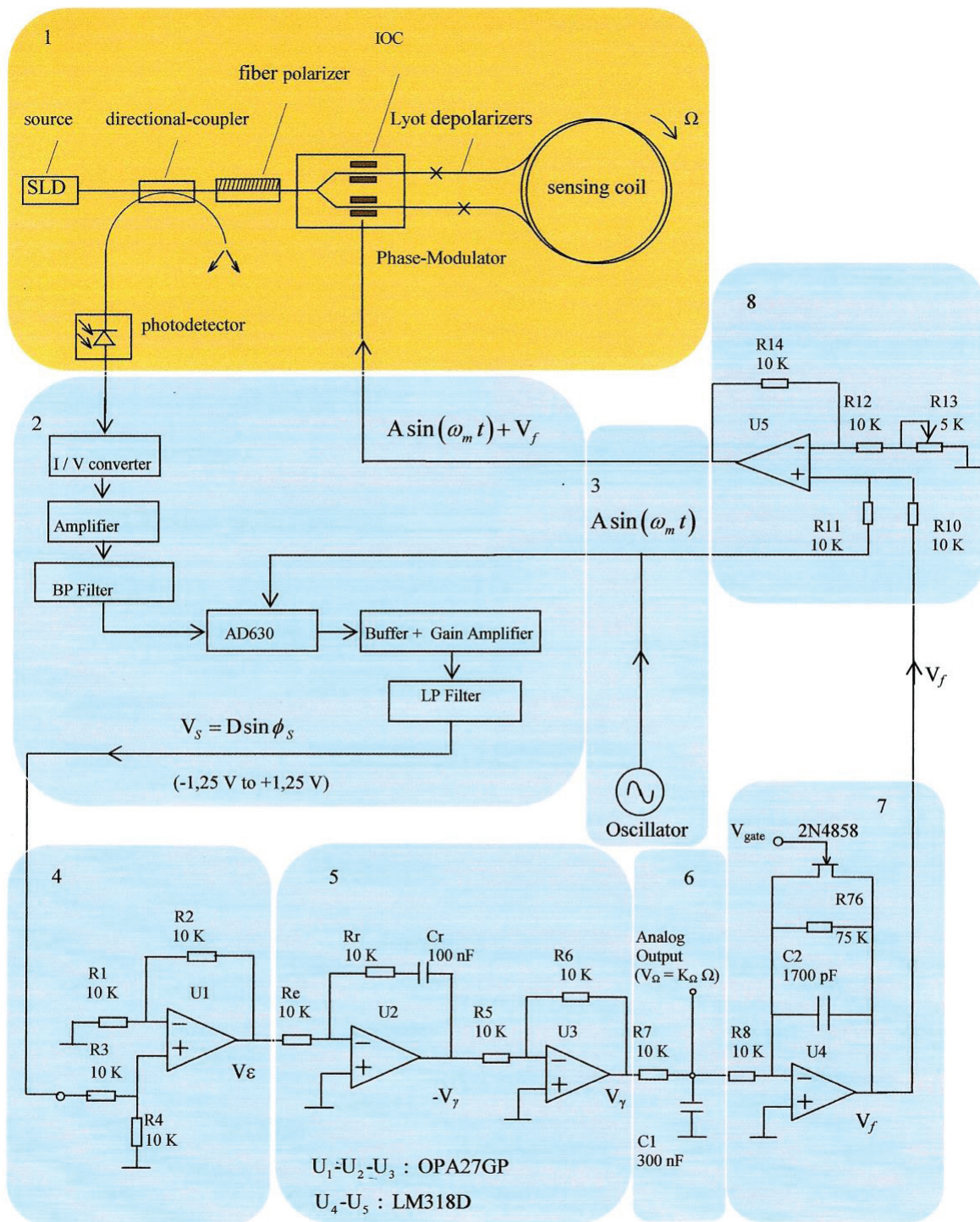
Figure 2. Analog closed-loop scheme for feedback phase-modulation configuration.

intended sawtooth voltage on feedback phase modulation chain as reported on previous designs by literature [25–27]. Working as feedback phase modulation signal, the analogical serrodyne wave presents two important advantages with regard to the sinusoidal-one: (a) it is possible to generate the serrodyne wave easily by means of a simple integrator circuit (Miller integrator) with simple and low-cost electronic components; (b) the phase cancellation process inside the control loop becomes simpler and more efficient.

In accordance with the interference principle, the light intensity at the photodetector optical input presents the following form (for sinusoidal phase-modulation):

$$I_d(t) = \frac{I_0}{2} [1 + \cos(\Delta\phi)] = \frac{I_0}{2} \left\{ 1 + \left[J_0(\phi_m) + 2 \sum_{n=1}^{\infty} J_{2n}(\phi_m) \cos(2n\omega_m t) \right] \right. \\ \left. \cos\phi_s - 2 \sum_{n=1}^{\infty} J_{2n-1}(\phi_m) \sin[(2n-1)\omega_m t] \sin\phi_s \right\} \quad (5)$$

being J_n the Bessel-function of the first kind of n th order. Here, $\Delta\phi$ represents the effective phase-difference of the two counter-propagating optical waves on sensing coil. This value results from the combined action of the phase-modulation process ($\phi_m = \phi_{bias} + \phi_f$) and the Sagnac phase shift induced by the rotation-rate (ϕ_s). The output signal of the photodetector, in photocurrent form, is proportional to the light intensity at its optical input. This photocurrent signal is converted to voltage with a transimpedance amplifier that is placed at the entry of demodulation circuit. The demodulation circuit takes the task of extracting the information of the Sagnac rotation-induced phase shift (ϕ_s). The corresponding voltage signal at its output (V_s) scales as sine-function of the effective Sagnac phase difference. The PI controller performs an integration of the V_s signal in time domain, so that a voltage signal (V_γ) is obtained; this signal growing almost linearly with the time. This latter signal is filtered by means of a low pass filter so that the corresponding output signal on voltage form (V_Ω) is a DC voltage value that is possible to consider to be almost proportional to the gyroscope rotation-rate Ω (when $\sin\phi_s \approx \phi_s$). Therefore, the analogical output voltage signal V_Ω constitutes the measurement of



- 1- Optical Subsystem
- 2- Demodulation Circuit
- 3- Reference-Signal Generator (sine-wave signal)
- 4- Analog-Comparator
- 5-Analog Integrator (PI Controller)+ Inverter
- 6- Low-Pass Filter
- 7- OPAMP Inverter Integrator
- 8- Analog-Adder Circuit

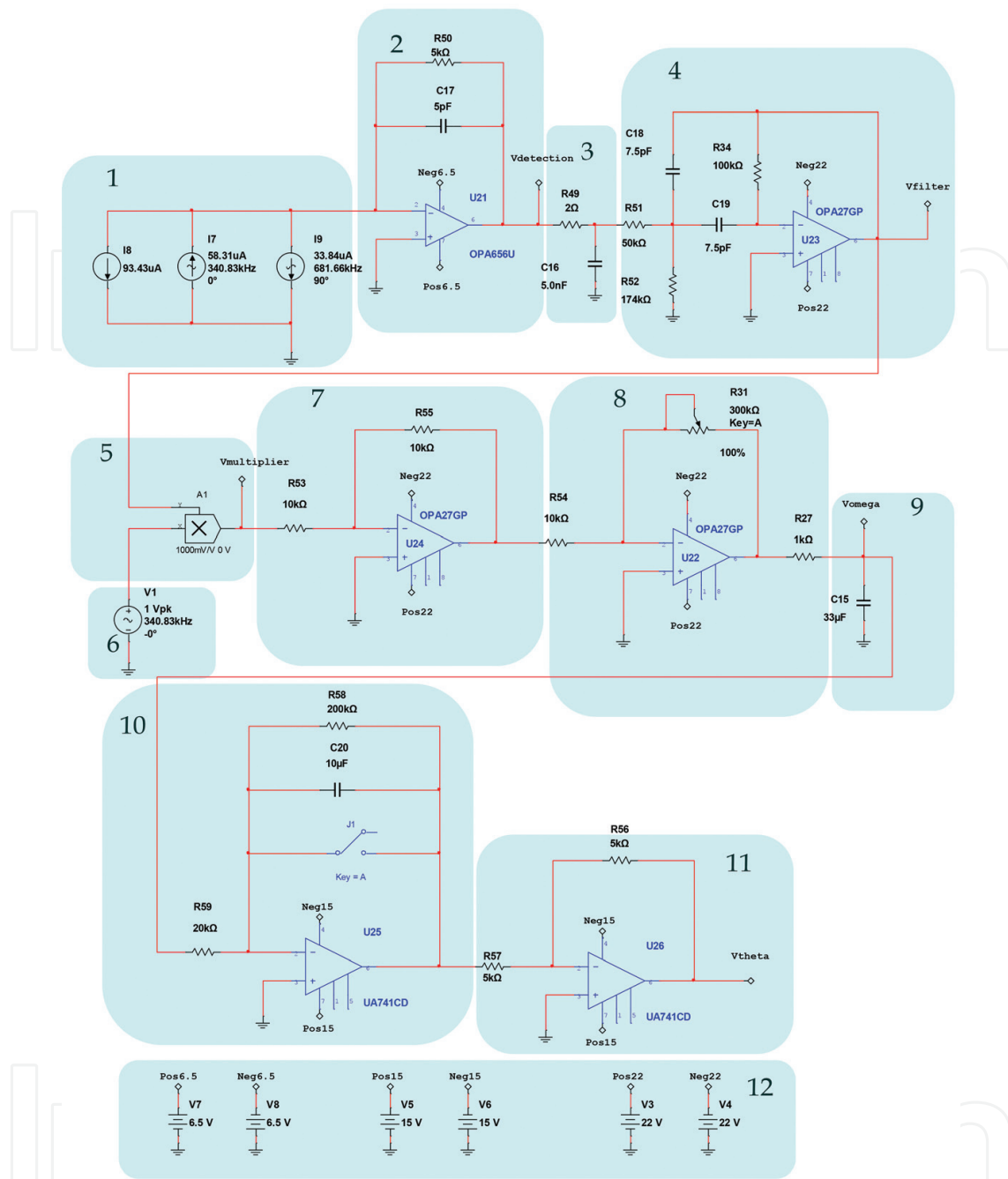
Figure 3. Block-diagram for electro-optical system and phase-sensitive-demodulation (PSD). The IFOG model is closed-loop configuration with sinusoidal-bias and serrodyne-feedback phase-modulations.

the rotation rate of the system. The control system, as a whole, acts as the principle of phase nulling. The phase-nulling process consists of generating a phase displacement ($\phi_m = \phi_{bias} + \phi_f$) in such a way that the phase-difference ϕ_f associated with the voltage output signal (V_f) is equal and with opposite sign with regard to the Sagnac phase-shift induced by the rotation rate, i.e., $\phi_f = -\phi_s$. To achieve this, the feedback phase modulation circuit holds a sample of the output signal V_Ω . Note that this voltage signal is obtained at the end of low pass filter (Block 6 on **Figure 3**) and is proportional to rotation-rate Ω . An integration operation is needed for obtaining a linear ramp voltage to apply on phase modulator. Then, it integrates and inverts this signal by means of an operational integrator-inverter circuit, turning this signal into the following form:

$$V_f = -\frac{1}{RC} \int_0^t V_\Omega dt \quad (6)$$

This way, the time variation of the voltage signal V_f is a linear ramp, being its slope proportional to the rotation rate of the system (V_Ω). **Figure 3** represents clearly the optical and electronic subsystems of the gyroscope, including the feedback phase-modulation and bias phase-modulation circuits for getting phase nulling process, both applied together to PM (Phase-Modulator). Referring now to **Figure 3**, then latter being the reference voltage for bias phase-modulation, see **Figure 2**), i.e., $V_m = V_{bias} + V_f$.

Therefore, the output signal of the phase modulator will be the sum of the phase-difference signals associated with the V_{bias} and V_f voltages, that is to say: $\phi_m = \phi_{bias} + \phi_f$. The error signal at the output of the comparator ($V_e \Delta\phi$) tends to be nulled in average-time, due to the phase-cancellation (the average-time of the reference bias phase-modulation ϕ_{bias} is 0). The feedback phase-modulation circuit consists of an AC sine-wave signal generator that produces a voltage reference signal V_{bias} at 340.83 kHz for bias phase modulation (block 3 of **Figure 3**), an analogical comparator circuit (differential-operational-amplifier, block 4 of **Figure 3**) that generates an error voltage signal V_e , an analogical Proportional-Integral (PI) Controller followed by one inverter-amplifier (block 5 of **Figure 3**), and a low-pass (LP) filter that yields a DC V_Ω voltage signal proportional to the rotation-rate (block 6 on **Figure 3**). The inverter-amplifier on block 5 produces the inversion of the $-V_e$ signal, obtaining the V_e voltage signal. The DC V_Ω output voltage after passive LP Filter on block 6 is integrated by integrator circuit on block 7 and then converted into the V_f feedback voltage signal, as calculated from Eq. (6), consisting on constant frequency and variable amplitude serrodyne wave which is applied to one of the two inputs of an analogical adder featured with a noninverter operational amplifier (the other input is connected to AC signal generator, block 8 on **Figure 3**). Therefore, the voltage output signal of this analogical adder is the V_m voltage signal that realizes the sum of the V_{bias} and V_f voltage signals, as described previously. **Figure 4** represents the detail block diagram of electronic scheme for detection and phase sensitive demodulation (PSD) circuits. It consists basically 12 functional blocks: (1) photodetector simulated output current, (2) transimpedance amplifier (current to voltage converter), (3) low-pass Filter (LP-Filter, $f_c = 800$ kHz), (4) band-pass-filter (BP Filter, $f_{center} = 340.83$ kHz), (5) analogical multiplier (AD630), (6) sinusoidal Oscillator ($f = 340.83$ kHz), (7) analogical inverter amplifier, (8) low-noise adjustable-gain



- | | |
|---|---|
| 1- Photodetector current simulation | 7- Analog-inverter amplifier |
| 2- Transimpedance amplifier | 8- Low noise adjustable gain amplifier |
| 3- LP Filter (fcutting = 800 kHz) | 9- Passive LP Filter (fcutting = 4,82 Hz) |
| 4- BP Filter (fcenter = 340.83 kHz) | 10- Analog Inverter-Integrator |
| 5- Analog Multiplier (AD630) | 11- Analog-Inverter Amplifier |
| 6- Oscillator (sinusoidal generator f = 340.83 kHz) | 12- DC Power Supply |

Figure 4. Detection and phase-sensitive-demodulation (PSD) circuits.

amplifier, (9) Low-Pass-Filter (LP Filter, $f_c = 4.82$ Hz) [28], (10) analogical integrator filter (for rotation-angle determination), (11) inverter OPAMP; the output voltage V_{theta} of this inverter allows obtaining the draft experienced by the system from a certain time (initialization time); and (12) DC power supplies. **Figure 5** represents in detail the analog PI controller and feedback phase modulation circuits. **Figure 6** represents the V_{gate} voltage signal generator circuit.

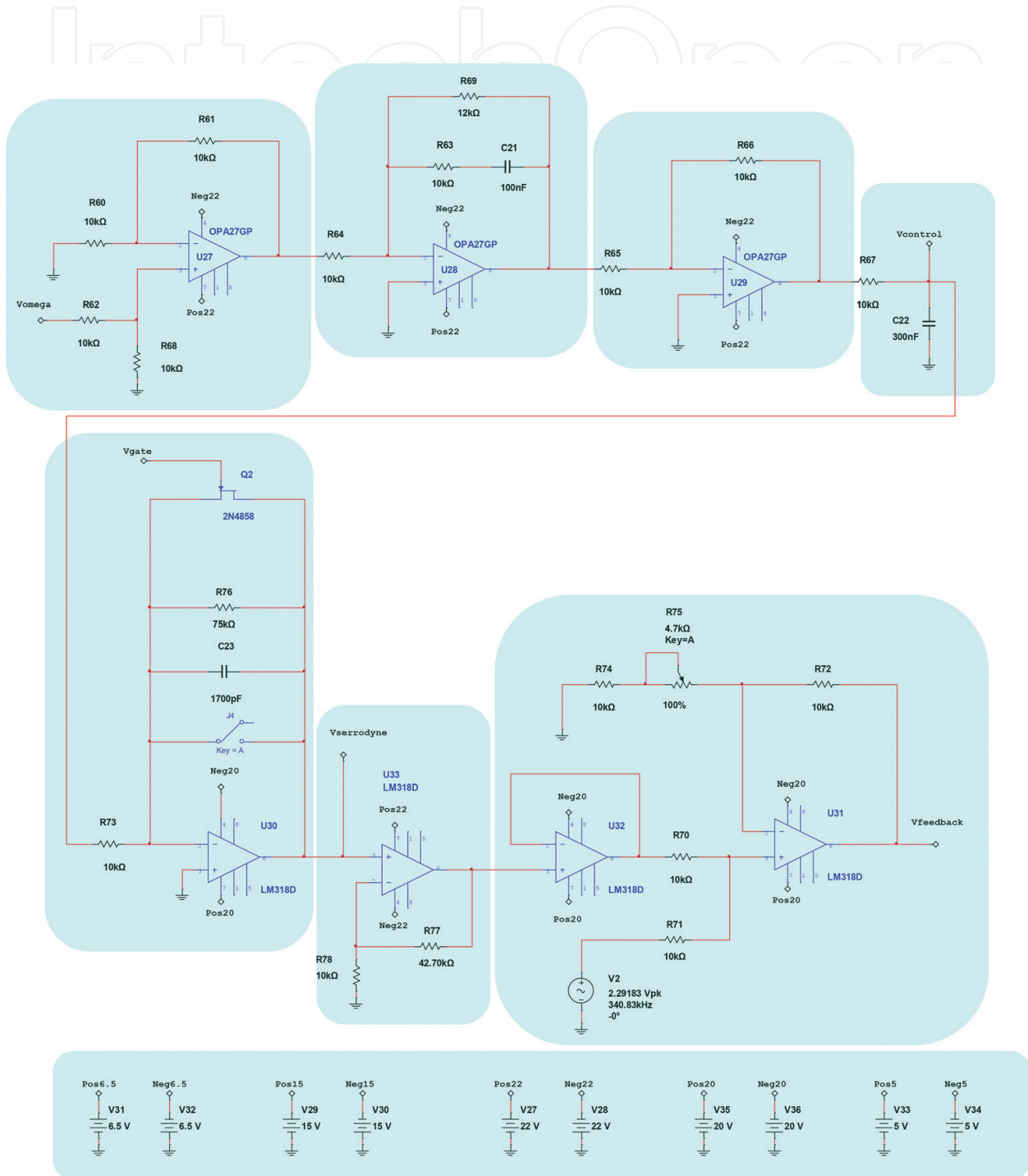


Figure 5. Analog controller circuit (includes blocks #1, #2, #3, and #4) and Serrrodyne feedback phase-modulation circuit (includes blocks # 5, #6, and #7).

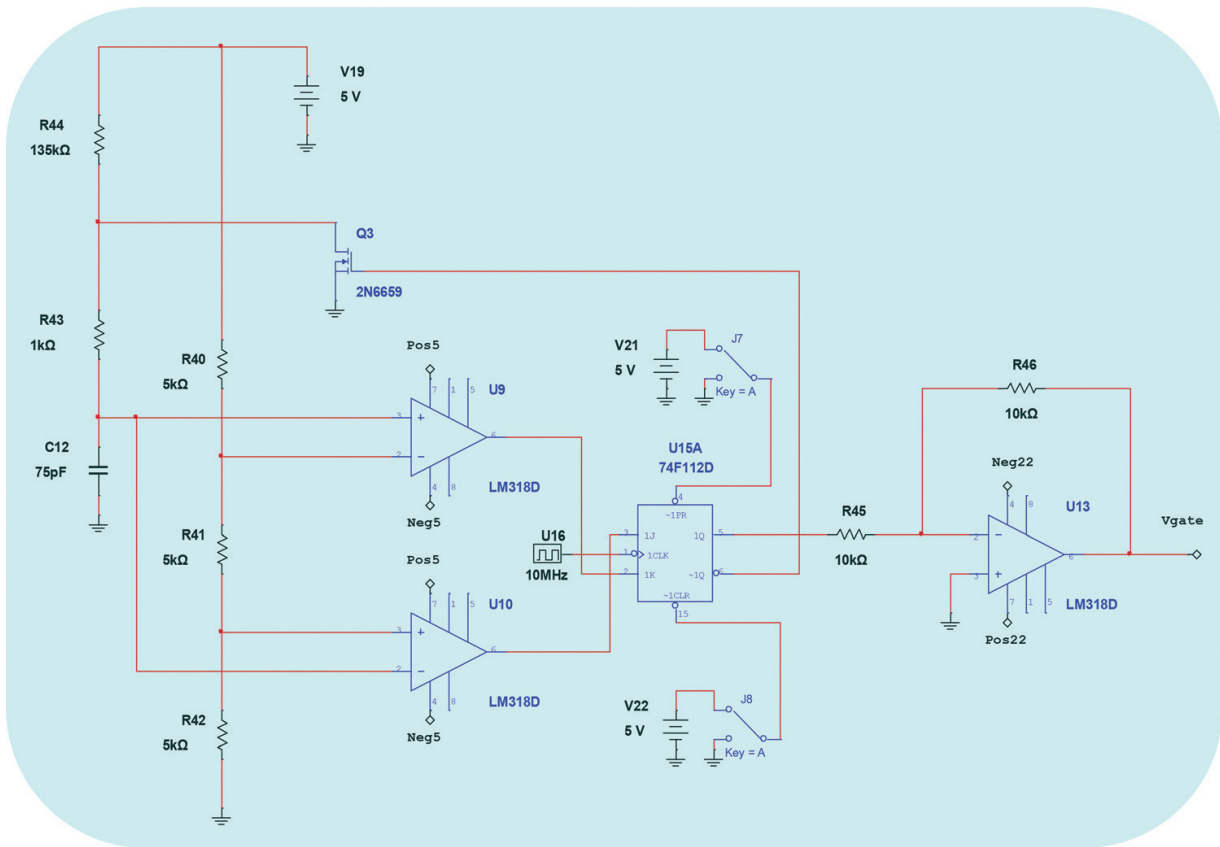


Figure 6. V_{gate} voltage signal generator (Astable pulse generator + J-K Flip-flop + analog inverter).

3. Calculations and estimations

This design has been simulated using Matlab-Simulink™ The MathWorks® and MultiSim™ National Instruments®. (Note that Synopsys® OptSim™ original version software only allows implementing APD-type photodetectors on optical circuit design, consequently an APD-PIN equivalent current-conversion will be necessary for connecting the simulation results to IFOG prototype designed in this article, which owes PIN photodetector). The open-loop scale factor K_0 can be calculated (being $c \approx 3 \times 10^8$ m/s the speed of light in vacuum) as:

$$K_0 = \frac{LD}{\lambda c} \tag{7}$$

The parameters of the model were chosen as fiber coil length $L = 300$ m, fiber coil diameter $D = 80$ mm, number of turns in the coil $N = 1194$, and light source wavelength $\lambda = 1310$ nm. The average optical-power at detector optical-input is $P_d = 145.61 \mu\text{W}$, and the responsivity of the InGaAs photodetector is $R = 0.68678 \mu\text{A}/\mu\text{W}$. The beat length of the optical fiber, L_{br} , can be calculated from its optical birefringence (B) as:

$$L_b = \frac{\lambda}{B} = \frac{\lambda}{|n_x - n_y|} \tag{8}$$

Parameter	Calculation Formula	Calculated Value	Estimated Value	Unit
Sensitivity threshold	$\Delta\Omega = \frac{2}{K_0} \sqrt{\frac{e}{P_d R t}}$	0.05193796	0.05193936	[°/hour]
Dynamic Range	$20 \log \left(\frac{\Omega_{max}}{\Omega_{min}} \right)$	101.38	101.38	[dB]
	$\Omega_{max} = \frac{\lambda c}{12LD}$	±78.185	±78.185	[°/s]
	$\Omega_{min} \approx \frac{\sqrt{hL_b}}{LD}$	±1.164×10 ⁻⁵	±1.164×10 ⁻⁵	[°/s]
Scale Factor	$SF = \frac{2\pi LD}{\lambda c}$	0.3837	0.3664	$\left[\frac{\text{rad}}{\left(\frac{\text{rad}}{\text{s}} \right)} \right]$

Table 1. Performance parameters of the designed IFOG prototype (analog closed-loop configuration).

where n_x and n_y are the refractive indexes of the two orthogonally polarized modes along the x and y directions. For this model, the following performance parameters have been analyzed: sensitivity threshold [29], dynamic range, and scale factor (SF) [30]. The values calculated (using the formulae) and estimated (by the results of the simulations) for such parameters are shown in **Table 1**. In this table, the third column shows the value calculated directly by the formula, and the fourth shows estimated results from the optical and electronic simulations.

The threshold sensitivity considers the SNR at photodetector optical input provided by the optical simulation, and the dynamic range and scale factor are determined by the sine function nonlinearity (assuming the maximum value $\phi_s = \pm\pi/6$). In the formulae, h is the h-parameter of the optical-fiber and t is the average integration time.

4. Simulation results

Three different kinds of computer simulations have been realized. First, the control system simulation has been realized using Matlab-Simulink™ for determining the 2% settling-time t_s of the complete electro-optic system. Second, an optical system simulation has been realized using Synopsys® OptSim™ for obtaining the optical interference signal at the PIN photodetector optical input and its main and representative values: average optical power and Signal-to-Noise-Ratio (SNR). Third and finally, the electronic circuit simulation made with MultiSim™ National Instruments® to obtain the V_Ω DC voltage as image of the rotation rate of the system and then for obtaining the output graph-response of gyroscope unit.

Figure 7 represents the parametric model of IFOG' electro-optical system. It is depicted as a parameterized block diagram corresponding to electro-optical system equivalent to the gyroscopic sensor. Here, it is taking into account the values of the parameters identified on its optical and electronics circuits. The system's step-response curve (obtained with Matlab-Simulink®) is shown in **Figure 8**. A settling time t_s (2%) of 1.39 ms is obtained. This value can be used to estimate a value for the initialization time of the final gyroscope unit. Results of optical subsystem simulation (realized by means of OptSim™ software) are represented on **Figures 9–14**. **Figure 9** represents the optical schematic circuit of the designed model for

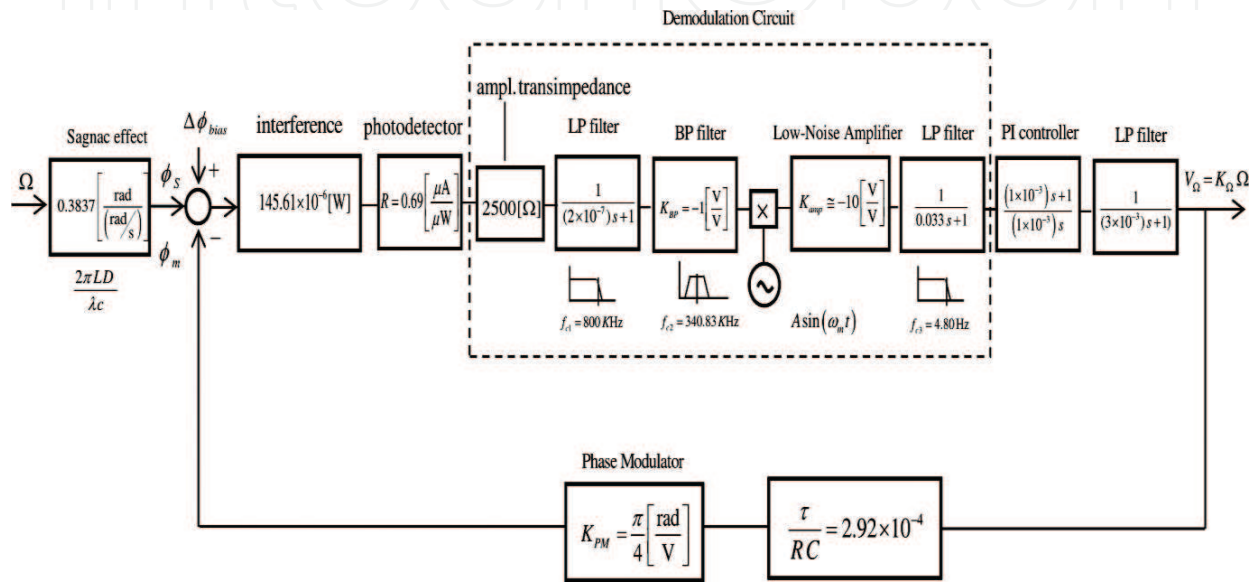


Figure 7. Parameterized block-diagram of the designed IFOG model considered as a continuous linear system (parameters: $L = 300$ m, $D = 0.08$ m, $\lambda = 1310$ nm, $P_d = 145.61$ μ W, $R = 0.69$ μ A/ μ W).

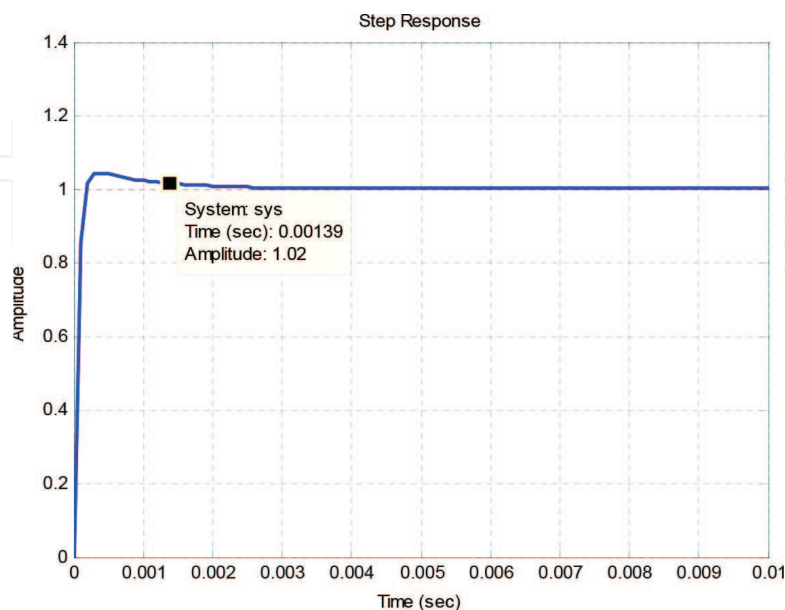


Figure 8. Time-response of the complete closed-loop system obtained for step-stimulus input signal (for step-stimulus input the t_s 2% settling time obtained is 1.39 ms).

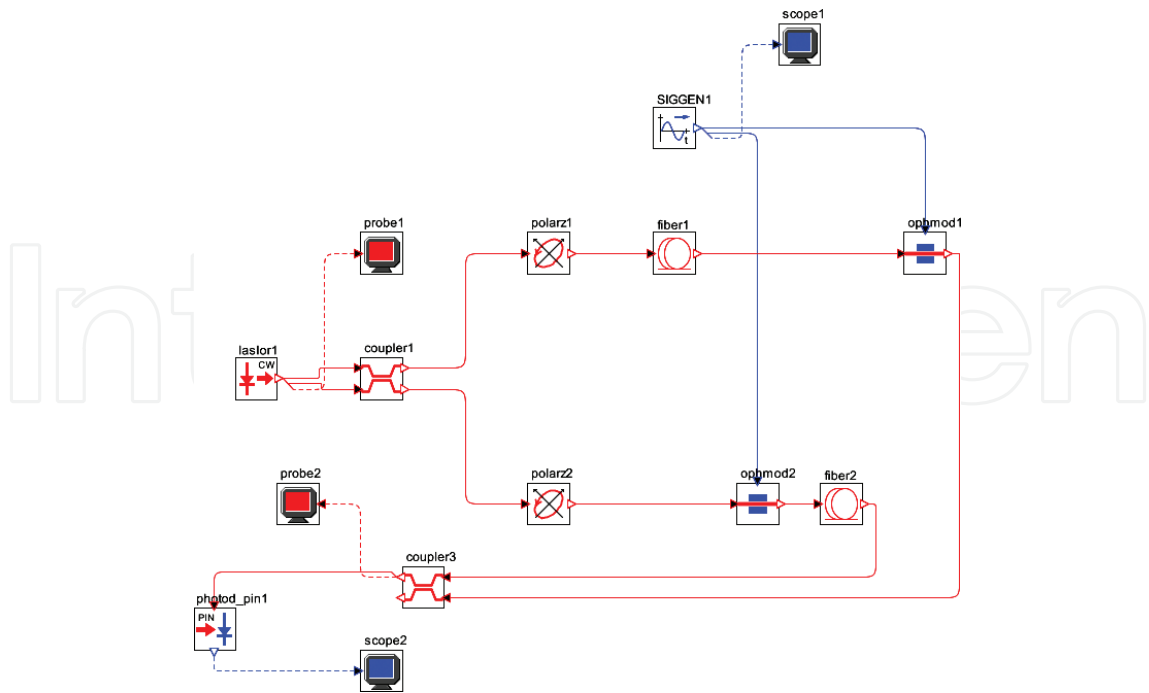


Figure 9. Optical circuit setup of the designed IFOG gyroscope for computer simulation (OptSim™).

obtaining its optical performance. Figure 10 represents the sinusoidal electrical signal provided by the AC signal generator and applied to the PM (Phase-Modulator) as bias phase-modulation signal. Figure 11 represents the optical-power spectrum at the photodetector optical input (central frequency is 288.844 THz).

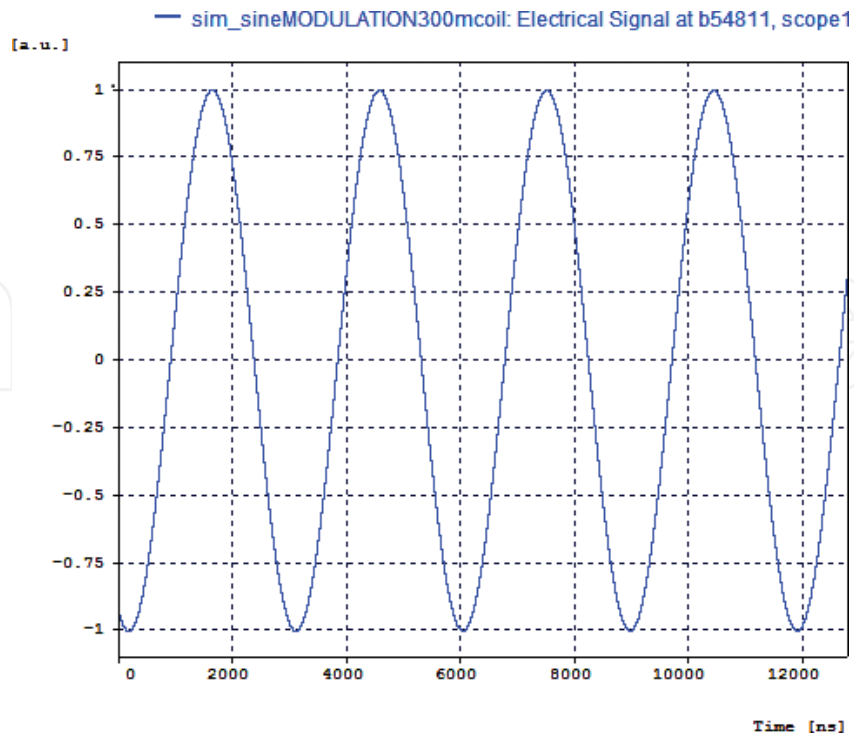


Figure 10. Sinusoidal voltage signal provided by AC signal generator and applied to PZT phase-modulator (PiezoZeramicTube).

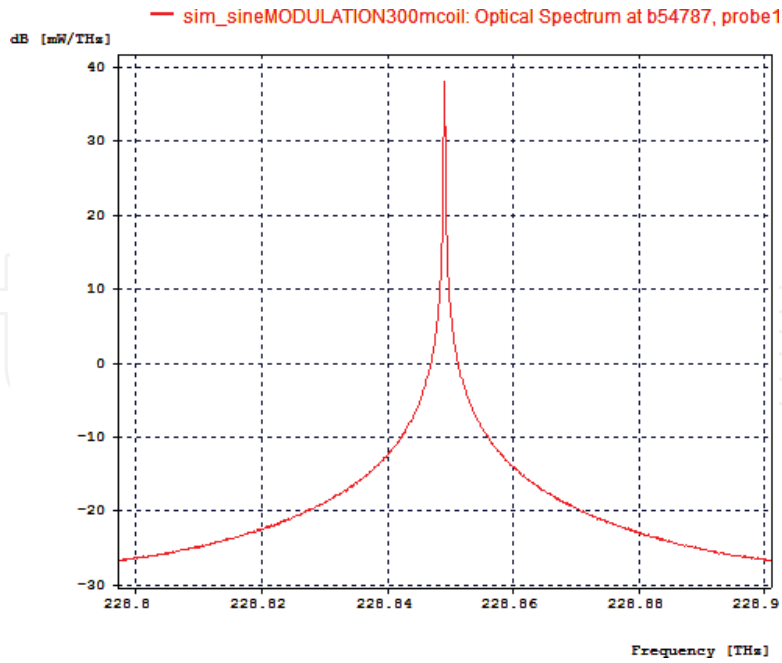


Figure 11. Optical-power spectrum obtained at photodetector optical-input.

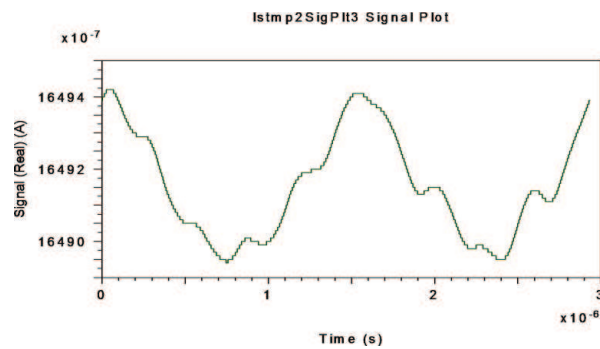


Figure 12. Interferometric signal at electrical output of APD-equivalent-photodetector (after electrical BP filter, $f_{center} = 340.83$ kHz) when $\Omega = \pm 10^\circ/s$ is applied to system.

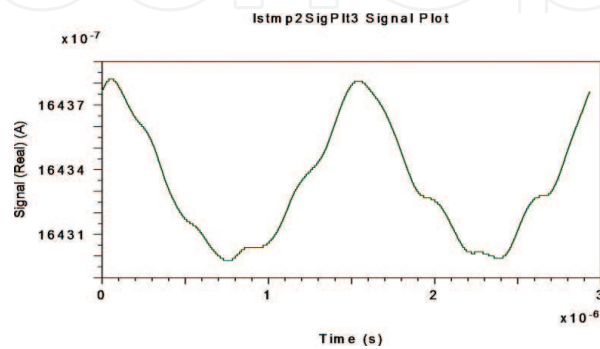


Figure 13. Interferometric signal at electrical output of APD-equivalent-photodetector (after electrical BP filter, $f_{center} = 340.83$ kHz) when $\Omega = \pm 20^\circ/s$ is applied to system.

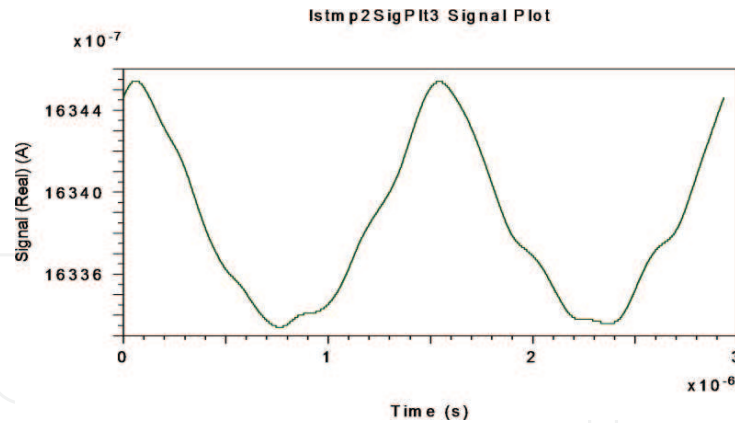


Figure 14. Interferometric signal at electrical output of APD-equivalent-photodetector (after electrical BP filter, $f_{center} = 340.83$ kHz) when $\Omega = \pm 30^\circ/s$ is applied to system.

Considering an input value of $210 \mu W$ as the average optical power value providing by light source, $145.61 \mu W$ were obtained at the optical input of photodetector, which means a power loss of -9.837808 dBm. Calculation of photon-shot-noise photocurrent at photodetector, taking into account $100 \mu A$ for average real value of photocurrent at its electrical output, is the following:

$$I_{sn} = \sqrt{\frac{e^2 q \lambda}{h c} P_{\max\text{-detector}} \Delta f} = \sqrt{\frac{(1.6 \times 10^{-19})^2 \times 0.65 \times (1310 \times 10^{-9})}{(6.624 \times 10^{-34}) \times (3 \times 10^8)}} \times (100 \times 10^{-6}) \times 1$$

$$= \sqrt{1.096940 \times 10^{-23}} = 3.312008 \times 10^{-12} \text{ A}$$

Note that lower the photon-shot-noise photocurrent value, lower is the threshold sensitivity of IFOG sensor and therefore also higher is its accuracy. On the other hand, it is needed to say that for low level of optical power coupled into photodetector, the main optical noise source of IFOG-sensor is photon shot noise (excess RIN can be neglected). This way, in accordance with photon-shot-noise photocurrent above calculated, the threshold sensitivity of gyro sensor (that is to say, the minimum rotation-rate which is able to measure) can be calculated as shown next (this value is collected in **Table 1**):

$$\Omega_{\lim} \cong \left(\frac{hc^2}{\pi e q L D P_{\max}} \right) I_{sn} = \left[\frac{6.624 \times 10^{-34} \times (3 \times 10^8)^2}{\pi \times (1.6 \times 10^{-19}) \times 0.65 \times 300 \times 0.08 \times (100 \times 10^{-6})} \right]$$

$$\times 3.312 \times 10^{-12} \approx 2.5180234 \times 10^{-7} \text{ [rad/sec]}$$

$$= 2.5180234 \times 10^{-7} \times \left(\frac{180^\circ}{\pi} \right) \times \left(\frac{3600 \text{ sec}}{1 \text{ hour}} \right) = 0.05193796 \text{ [^\circ/hour]}$$

Figures 12–14 represents the electrical interferometric signal (in APD photo-current form, after electrical BP filtering, $f_{center} = 340.83$ kHz) detected by an APD equivalent photodetector, when $\Omega = \pm 10^\circ/s$, $\Omega = \pm 20^\circ/s$, and $\Omega = \pm 30^\circ/s$, respectively, are applied to the system. This is because the block-mode simulation only offers measurements realized by an APD equivalent

photodetector as optical output of the system. The average mean values of APD photo-currents are, respectively, 1649.20 μA , 1643.30 μA and 1633.80 μA , which correspond to 99.873 μA , 99.515 μA and 98.940 μA for PIN-equivalent photodiode. Note that in this interval, the average current decreases almost linearly as rotation-rate increases linearly. These curves agree with theoretical interferometric curves as calculated on optical input photodetector.

The results of electronic circuits' simulation (realized by MultiSim™ software) collect the waveforms voltage on the following test-point voltage: $V_{detection}$, V_{filter} , $V_{multiplier}$, V_{thetar} , $V_{serrodyne}$, and V_{gate} (referring to **Figures 4–6**). All these values are obtained on electronic circuits when $\Omega = + 30^\circ/\text{s}$ rotation-rate is applied to system and are gathered on **Figures 15–20**. **Figure 15** shows the detected output voltage after transimpedance amplifier ($V_{detection}$, see **Figure 4**). **Figure 16** represents the output voltage after BP Filter (V_{filter} , see **Figure 4**). **Figure 17** represents output voltage after analog Multiplier ($V_{multiplier}$, **Figure 4**). **Figure 18** represents output voltage after Angle analog integrator (V_{thetar} , **Figure 4**). **Figure 19** represents output voltage after analog integrator ($V_{serrodyne}$: a sawtooth-voltage with constant frequency and variable amplitude, this amplitude depending on V_Ω voltage value). Finally, **Figure 20** represents V_{gate}

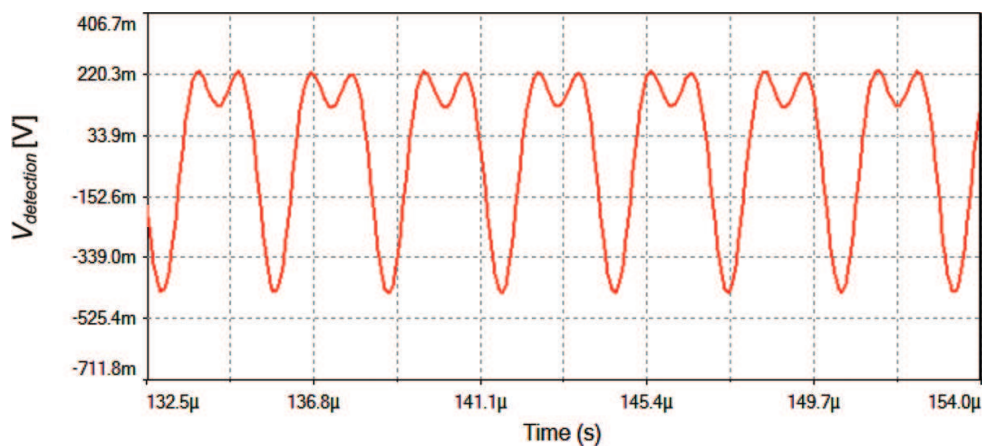


Figure 15. $V_{detection}$ voltage signal (after transimpedance amplifier) for $\Omega = + 30^\circ/\text{s}$ when $\Omega = \pm 30^\circ/\text{s}$ is applied to system.

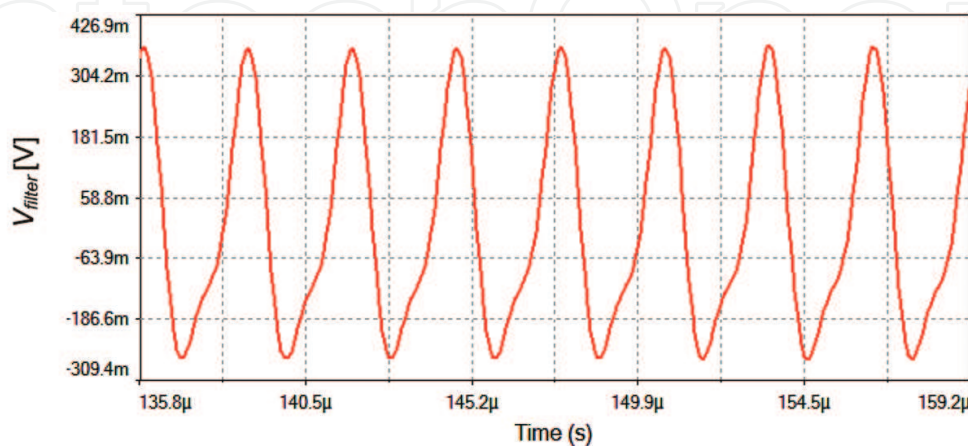


Figure 16. V_{filter} output voltage after BP filter for $\Omega = + 30^\circ/\text{s}$.

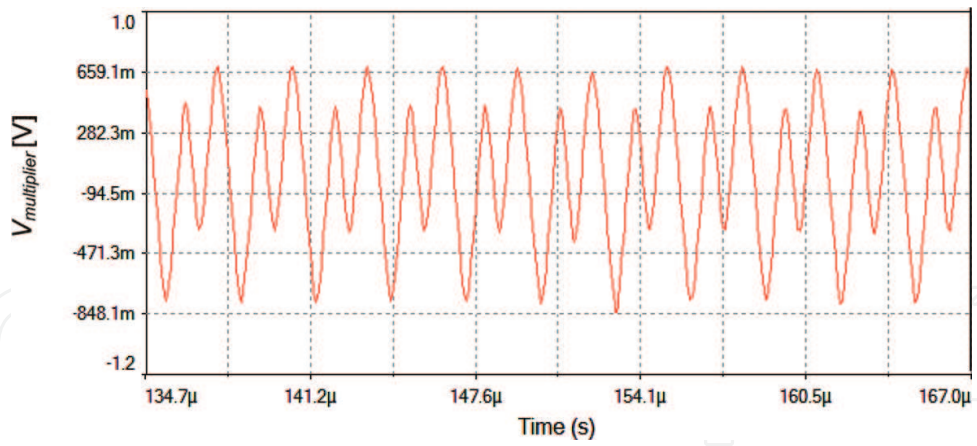


Figure 17. $V_{multiplier}$ output voltage after AD630 analog multiplier for $\Omega = + 30^\circ/s$.

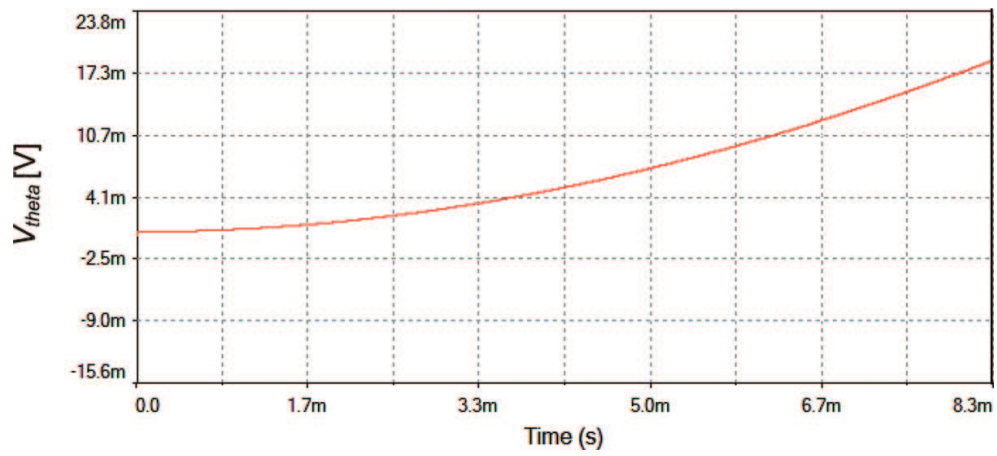


Figure 18. V_{theta} output voltage after angle analog integrator for $\Omega = + 30^\circ/s$.

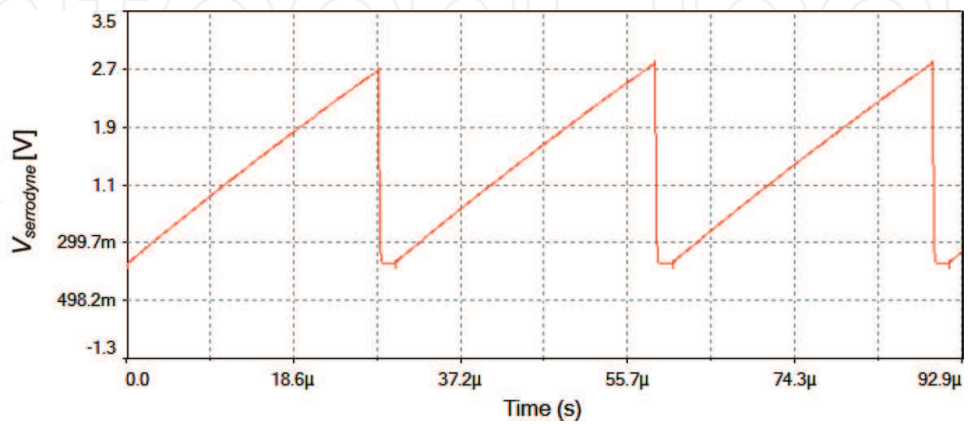


Figure 19. $V_{serrodyne}$ at analog integrator output (feedback-voltage signal to phase-modulator) for $\Omega = + 30^\circ/s$.

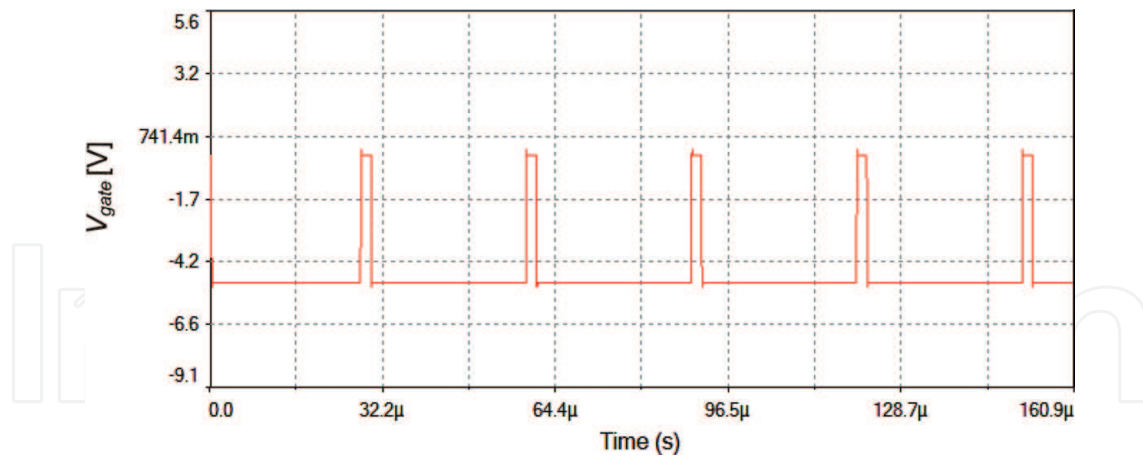


Figure 20. V_{gate} voltage generated by pulse generator circuit (fixed frequency $f = 32.59$ kHz).

generated by pulse generator circuit and applied to gate of J2 N4858 FET transistor (see the circuit on **Figure 6**).

The expansion of Eq. (5) with only the contribution of first two time-component harmonics allows obtaining an approximate value for detected $I_d(t)$ photo-current. The result of this approximation is:

$$I_d(t) \cong \frac{I_0}{2} [1 + J_0(\phi_m) \cos \phi_S] + I_0 J_2(\phi_m) \cos(2\omega_m t) \cos \phi_S - I_0 J_1(\phi_m) \sin(\omega_m t) \sin \phi_S \quad (9)$$

being I_0 the maximum value of detected photo-current and ϕ_m the amplitude of differential phase-modulation. Assuming the $\phi_m = 1.80$ value, this value corresponding to the maximum value of function $J_1(\phi_m)$, the following Bessel functions calculations are obtained:

$$J_0(1.80) \cong 0.33999, J_1(1.80) \cong 0.58150 \text{ and } J_2(1.80) \cong 0.30611.$$

then, taking into account $100 \mu\text{A}$ as the DC average detected photodetector-current and after some numerical adjusts, Eq. (9) yields the following analytical value:

$$I_d(t) \cong 74.63 [1 + 0.34 \cos \phi_S] + 45.69 \cos(2\omega_m t) \cos \phi_S - 86.79 \sin(\omega_m t) \sin \phi_S \quad [\mu\text{A}] \quad (10)$$

This analytical expression allows to calculate for every rotation-rate Ω value (i.e., ϕ_S Sagnac phase shift) the DC term and the first and second harmonics terms. These terms can later be introduced as current DC and AC generators on MultiSim™ circuit simulation program (block 1 on **Figure 4**). By this means, V_Ω can be measured on simulated circuit (see **Figure 4**), so that a table with V_Ω value versus Ω [$^\circ/\text{s}$] value can be made. **Table 2** lists the correlation data obtained from the electronic demodulation circuit for the measured output-voltage signal V_Ω [mV] versus input rotation rate Ω [$^\circ/\text{s}$] of the system for full dynamic range (0 to $\pm 78.19 \approx \pm 80$ [$^\circ/\text{s}$]) with a step of $10^\circ/\text{s}$. **Figure 21** shows the graphic relationship between both variables corresponding to mentioned data table. After performing the appropriate calculations, taking into account the theoretical value of the SF (Scale Factor) of the gyroscope that appeared on **Table 1**, a linear

Ω [°/s]	0	±10	±20	±30	±40	±50	±60	±70	±80
V_{Ω} [mV]	0	±305	±613	±931	±1280	±1609	±1970	±2337	±2708
$(V_{\Omega})_{lin}$ [mV]	0	±338.7	±677.5	±1016	±1355	±1694	±2032	±2371	±2710
$ \Delta(V_{\Omega}) $ [mV]	0	33.73	64.46	85.19	74.92	84.65	62.38	34.11	1.834
$ \Delta(V_{\Omega}) / (V_{\Omega})_{lin} $ %	0	9.959	9.514	8.385	5.529	4.997	3.070	1.439	0.068

Table 2. Output data and linear fitting for $0 \div \pm 80^\circ/\text{s}$ (full dynamic range), step = $10^\circ/\text{s}$.

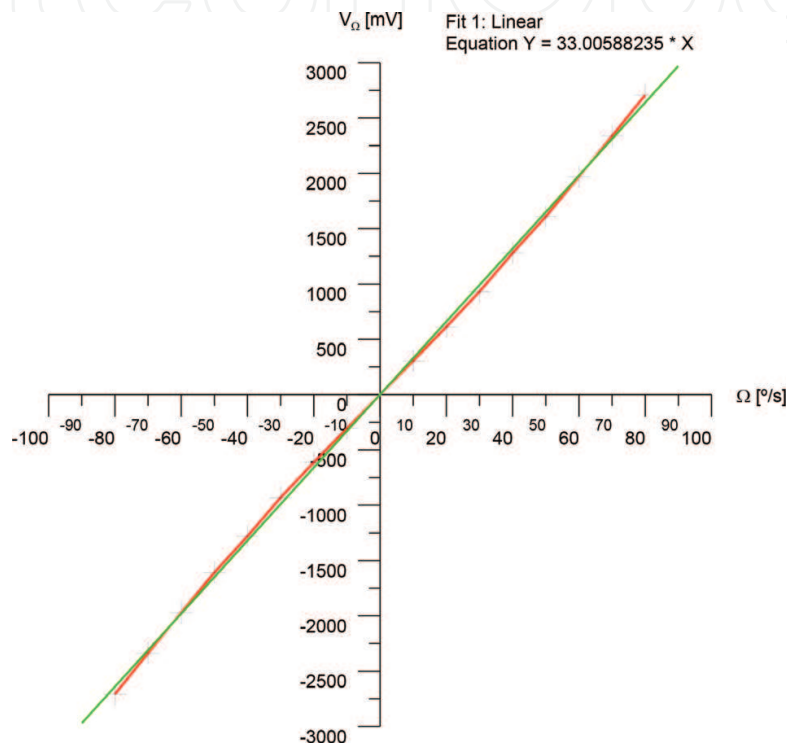


Figure 21. Output response curve V_{Ω} [mV] versus Ω [°/s] (in red color) and linear fitting (in green color) for 0 to $\pm 80^\circ/\text{s}$ (full dynamic range).

function can be obtained for the best fitting of the output response curve. This way, it is possible to evaluate the linearity of this graphic and then assuming this value as scale factor linearity of the IFOG-model. **Tables 3** and **4** are constructed to obtain detailed scale-factor linearity analysis in more restricted dynamic ranges.

Ω [°/s]	0	±1	±2	±3	±4	±5	±6	±7	±8	±9	±10
V_{Ω} [mV]	0	±30	±59	±90	±120	±150	±180	±210	±240	±270	±305
$(V_{\Omega})_{lin}$ [mV]	0	±30.13	±60.26	±90.39	±120.52	±150.65	±180.78	±210.91	±241.04	±271.17	±301.30
$ \Delta(V_{\Omega}) $ [mV]	0	0.13	1.26	0.39	0.52	0.65	0.78	0.91	1.04	1.17	3.70
$ \Delta(V_{\Omega}) / (V_{\Omega})_{lin} $ %	0	0.431	2.091	0.431	0.431	0.431	0.431	0.431	0.431	0.431	1.228

Table 3. Output data and linear fitting for $0 \div \pm 10^\circ/\text{s}$ (restricted dynamic range), step = $1^\circ/\text{s}$.

Ω [°/s]	0	±0.1	±0.2	±0.3	±0.4	±0.5	±0.6	±0.7	±0.8	±0.9	±1.0
V_{Ω} [mV]	0	±3	±6	±9	±12	±15	±18	±21	±24	±27	±30
$(V_{\Omega})_{lin}$ [mV]	0	±3	±6	±9	±12	±15	±18	±21	±24	±27	±30
$ \Delta(V_{\Omega}) $ [mV]	0	0.0	0.0	0.0	0.0	0.0	0.0	0.0	0.0	0.0	0.0
$ \Delta(V_{\Omega}) / (V_{\Omega})_{lin} $ %	0	0.0	0.0	0.0	0.0	0.0	0.0	0.0	0.0	0.0	0.0

Table 4. Output data and linear fitting for $0 \div \pm 1$ °/s (restricted dynamic range), step = 0.1°/s.

Table 3 shows data obtained for 0 to ±10 [°/s] dynamic range with a step of 1°/s, and **Figure 22** shows the corresponding V_{Ω} versus Ω graphical representation. **Table 4** shows data obtained for 0 to ±1 [°/s] dynamic range with a step of 0.10°/s, and **Figure 23** shows the corresponding V_{Ω} versus Ω graph. **Tables 2–4** also includes the values $(V_{\Omega})_{lin}$ [mV] of the correspondent linear fitting, the module of the differential values $\Delta(V_{\Omega})$ [mV], and the module $|\Delta(V_{\Omega}) / (V_{\Omega})_{lin}|$ of the ratio values.

The $\Delta(V_{\Omega})$ [mV] value is defined as:

$$\Delta V_{\Omega} = V_{\Omega} - (V_{\Omega})_{lin} \text{ [mV]} \tag{11}$$

from correlation values of both curves (output data curve and linear fitting curve), it can be determined the non-linearity percentage coefficient of the SF, defined as the percentage of the standard deviation, which can be calculated by the following expression:

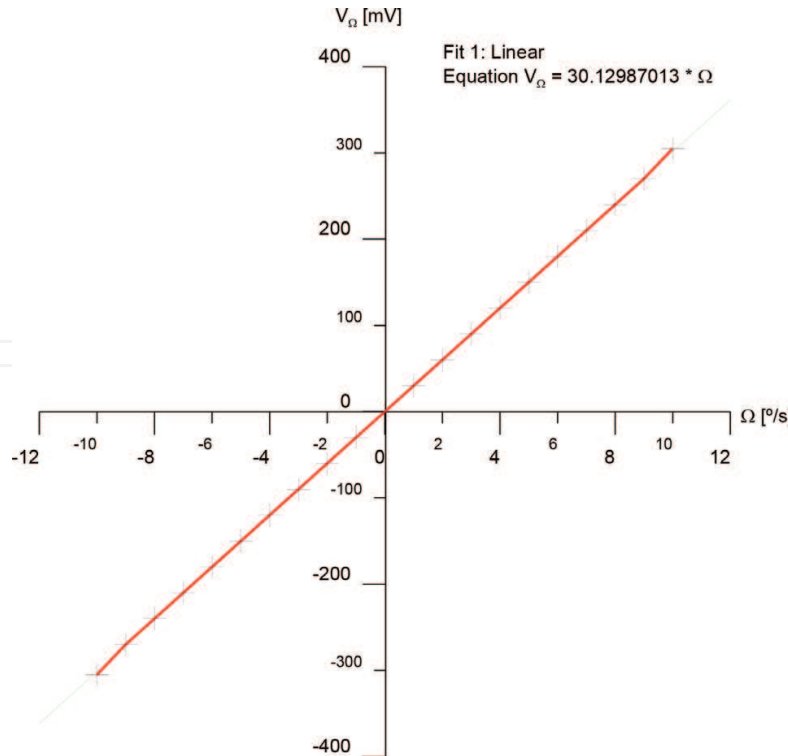


Figure 22. Output response curve V_{Ω} [mV] versus Ω [°/s] (in red color) and linear fitting (in green color) for 0 to ±10°/s (restricted dynamic range).

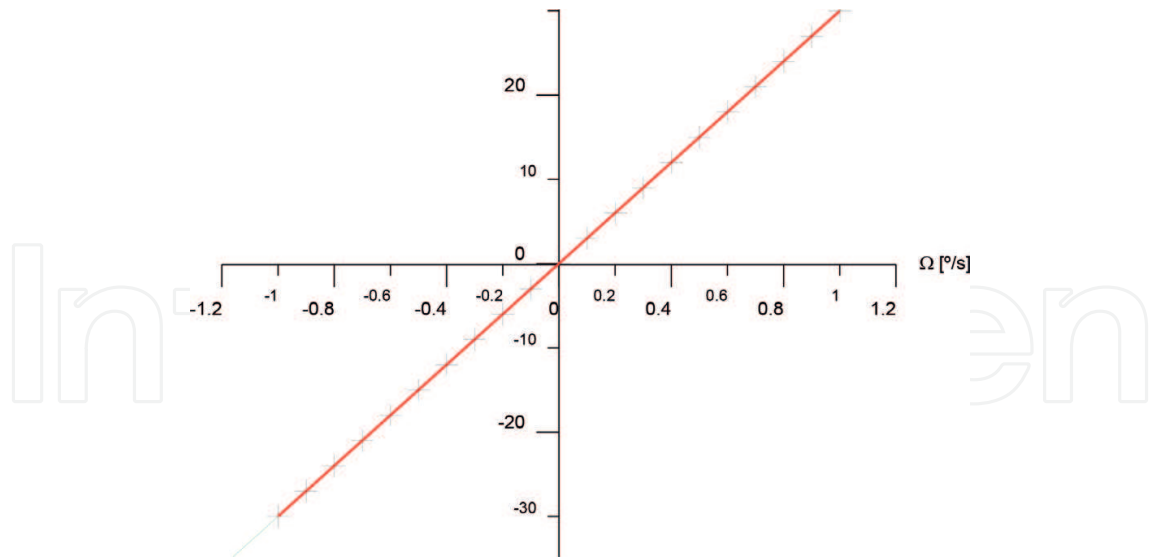


Figure 23. Output response curve V_{Ω} [mV] versus Ω [$^{\circ}/s$] and linear fitting (in green) for 0 to $\pm 1^{\circ}/s$.

$$SF - NonLinearity(\%) = \sqrt{\frac{1}{N} \sum_{n=1}^N \left| \frac{(\Delta V_{\Omega})_i}{(V_{\Omega \text{ lin}})_i} \times 100 \right|^2} \quad (12)$$

so that in our case, for full dynamic range with $N = 17$ and taking the values obtained from **Table 2**, this expression yields a value of 4.386%. For **Table 3** Eq. (12) reaches the value of 0.838% and for **Table 4** its value is 0.0%. These values agree with those obtained for commercial IFOG units of similar characteristics.

5. Discussion of simulation results

The results obtained for the performance parameters of the gyroscope model designed in this article (threshold sensibility = $0.052^{\circ}/h$, dynamic range = $\pm 78.19^{\circ}/s$, scale factor nonlinearity = 4.836%) are sufficient for intermediate grade gyroscopic applications, such as stabilization, pointing, and positioning of mobile platforms or inertial-navigation systems for terrestrial robots and automotive vehicles [31–36].

The effects of the different types of optical noise [37–50] which take place are not critical in the specific design of this sensor, since its operation works in a medium level of optical-power and the signal-to-noise-ratio (SNR) is relatively high at photodetector's optical-input (SNR > 100 dB). The most important type of optical-noise for this sensor is photon-shot-noise on photodetector, with a 3.31 pA noise-equivalent-current value, this value being much less than 100 μA that is the average photocurrent value for photodetector electrical output signal, in zero rotation-rate conditions. This type of noise is not susceptible of correction, since it owes to intrinsic

quantum-mechanical mechanism of photoconductivity (electron–hole production by photonic shoot).

The relative intensity noise (RIN) is an important issue in this design, since it works at a medium-level of average optical-power coupled to photodetector optical-input (145.61 μW average optical-power value). This type of noise stems from two causes: (1) the two interfering optical waves do not come to photodetector with the same optical power level, due to polarization crosstalk between the two orthogonal polarizations states along the entire length of sensing fiber-coil (due to fiber-birefringence phenomenon), and (2) the light source is low-coherence (broadband source), thereby producing several beat wavelengths, which add at photodetector optical-input, causing a variation in relative intensity on every point of photodetector's response-curve. This noise can be minimized by reducing the optical power emitted by light source. But a very large reduction in optical power also lowers the SNR at the photodetector, so that to maintain it at a high level, the optical power emitted by light source cannot be reduced greatly.

The noise associated with the fiber nonlinear Kerr effect is based on the electro-optical phenomenon which consists in changes experienced by refractive index of the optical fiber caused when it is excited by an optical wave that varies in amplitude. This occurs by the fluctuation of the optical power level of light source. In the case of the gyroscopic system, this optical power variation coupled to the fiber coil causes changes on its refractive index, which results in a phase change in the optical wave propagated along the length of the optical fiber coil. This change can be evaluated as a phase-equivalent noise and could be diminished efficiently using a low coherence light source (broadband source). Another important aspect is providing the light source with a thermal stabilization system to achieve a constant level of optical power emission.

The Shupe thermal effect is due to local temperature gradients along the fiber coil length. These temperature gradients induce phase changes in the optical waves traveling through the fiber. This effect can be minimized performing an appropriate winding of fiber-coil, so that a uniform temperature distribution is achieved throughout its entire length. The quadrupolar winding (number of turns in each layer of coil equal to an integer multiple of four) fulfills this condition. Other minor optical noise sources with less effect on the optical signal detected by photodetector are due to backscattering and reflections phenomena along the length of the sensing fiber-coil. A serious disadvantage for this model design is that the results of optical simulation do not allow realizing the evaluation of the main sources of optical noise.

Regarding the electrical noise generated by the electronic circuits, the most important is white noise (thermal-noise or Johnson noise), which spreads equally over all the frequencies. An appropriate way for overcoming this noise source is performing a selective filtering at the frequency of the desired signal and fitting later the gain of the amplification stages to increase the electrical SNR at the output. In the case of the designed IFOG circuits, a strict design of LPF (Low-Pass-Filter) and BPF (Band-Pass-Filter) is necessary after photodetector-amplifier. It is crucial for obtaining a good scale-factor linearity of designed IFOG-model. It is due to the fact that it depends on linearity of the obtained V_{Ω} versus Ω graphical representation derived from signal demodulation process.

6. Conclusions

An IFOG prototype was theoretically designed by means of simulating tools. The conventional IFOG design with sinusoidal phase modulation is based on open-loop configuration. The main innovation of IFOG-design presented here is the use of a simple closed-loop electro-optical configuration, realized by means of optical and electronic cost competitive components. Furthermore, the proposed design also allows to reach substantial progress in stability and linearity of the Scale Factor (SF), dynamic range and threshold sensitivity of the gyroscope, compared to previous models proposed with the same fiber-optic coil length ($L = 300$ m). The cost advantage in optical subsystem is obtained by means of a design with depolarization of optical waves, by using two Lyot depolarizers, both realized in optical fiber. This allows using a sensing coil made in optical standard fiber, instead of a special polarization maintaining fiber, which is much more expensive. On the other hand, the electronic circuit subsystems (detection, demodulation, and feedback signal processing) is based on a conventional analog design, using classic electronic components which are high precision and cost competitive, so that it also contributes to achieving a reasonable cost and at the same time optimizing quality/price ratio of final device. An interesting observation regarding to cost is that if the entire volume occupied by the device does not suppose a major restriction (this condition is fulfilled in certain applications), it is possible to get an additional saving cost by means of a particular design of optical subsystem. This design can be based on a suitable selection of bulk optical components: the Integrated Optical Circuit (IOC) can be replaced with two 2×2 fiber optical couplers (SMF fiber), a fiber polarizer, and a fiber-based electro-optic phase modulator (PZT), since until the day the IOC is not standard-manufacture. The same way, for light source it is possible using a low-power and limited-consumption laser, as an Erbium-Doped-Fiber-Amplifier (EDFA), and for depolarization of the optical wave a new solution based on bulk optics can be adopted, such as crystal Lyot depolarizers.

Author details

Ramón José Pérez Menéndez

Address all correspondence to: ramonjose.perez@lugo.uned.es

UNED-Spain, Lugo, Spain

References

- [1] Lefèvre HC. *The Fiber-Optic Gyroscope*. Second ed. Boston-London: Artech House; 2014
- [2] Ezekiel S, Arditty HJ. *Fiber-Optic Rotation Sensors*. Berlin: Springer-Verlag; 1982
- [3] Lawrence A. *Modern Inertial Technology: Navigation, Guidance, and Control*. 2nd ed. New-York: Springer-Verlag; 1992

- [4] Sagnac G. L'ether luminex demontre par l'effect du vent relatif d'ether dans un interferometre en rotation uniforme. *Comptes Rendus de l'Académie des Sciences*. 1913;**95**:708-710
- [5] Sagnac G. Sur la preuve de la realité de l'ether luminex par l'experience de l'interferographe tournant. *Comptes Rendus de l'Académie des Sciences*. 1913;**95**:1410-1413
- [6] Hariharan P. Sagnac or Michelson-Sagnac interferometer. *Applied Optics*. 1975;**14**(10): 2319-2321
- [7] Bergh RA, Lefevre HC, Shaw HJ. Overview of fiber-optic gyroscopes. *IEEE Journal of Lightwave Technology*. 1994;**LT-2**:91-107
- [8] Bergh RA, Lefevre HC, Shaw HJ. All-single-mode fiber-optic gyroscope. *Optics Letters*. April 1981;**6**(4):198-200
- [9] Moeller RP, Burns WK, Frigo NJ. Open-loop output and scale factor stability in a fiber-optic gyroscope. *Journal of Lightwave Technology*. Feb. 1989;**7**(2):262-269
- [10] Bohm K, Petermann K. Signal processing schemes for the fiber-optic gyroscope. *Proceedings of SPIE, Fiber Optic Gyros: 10th Anniversary Conf*. 1986:36
- [11] Burns WK et al. Fiber-optic gyroscopes with depolarized light. *Journal of Lightwave Technology*. 1992;**10**(7):992-998
- [12] Szafraniec B et al. Theory of polarization evolution in Interferometric fiber-optic depolarized gyros. *Journal of Lightwave Technology*. 1999;**17**(4):579-590
- [13] Kintner EC. Polarization control in optical-fiber gyroscopes. *Optics Letters*. 1981;**6**(3):154-156
- [14] Sanders GA, Szafraniec B. Progress in fiber-optic gyroscope applications II with emphasis on the theory of depolarized gyros. *AGARD/NATO Conf. Report on Optical Gyros and Their Applications, AGARDograph*. 1999;**339**:11/1-1142
- [15] Pavlath GA. Productionization of fiber gyros at Litton guidance and control systems. *SPIE Proceedings*. 1991;**1585**:2-5
- [16] Sanders GA, Szafraniec B, Liu R-Y, Laskoskie C, Strandjord L. Fiber optic gyros for space, marine and aviation applications. *SPIE Proceedings*. 1996;**2837**:61-71
- [17] Patterson RA, Goldner EL, Rozelle DM, Dahlen NJ, Caylor TL. IFOG technology for embedded GPS/INS applications. *SPIE Proceedings*. 1996;**2837**:113-123
- [18] Lefèvre HC et al. Integrated Optics: a Practical Solution For The Fiber-Optic Gyroscope. *Proc. SPIE 0719, Fiber Optic Gyros: 10th Anniversary Conf*. 101, March 11, 1987. 101-112. DOI: 10.1117/12.937545
- [19] Kim BY et al. Response Of Fiber Gyros To Signals Introduced At The Second Harmonic Of The Bias Modulation Frequency. *Proc. SPIE 0425, Single Mode Optical Fibers*, 86, November 08 1983. DOI: 10.1117/12.936218
- [20] Kim BY et al. Gated phase-modulation feedback approach to fiber gyroscopes. *Optics Letters*. 1984;**9**(6):263-265

- [21] Kim BY et al. Gated phase-modulation feedback approach to fiber gyroscopes with linearized scale factor. *Optics Letters*. 1984;**9**:375-377
- [22] Kim BY et al. Phase reading all-fiber-optic gyroscope. *Optics Letters*. 1984;**9**:378-380
- [23] Böhm K et al. Signal processing schemes for the fiber-optic gyroscope. *Proc. SPIE 0719, Fiber Optic Gyros: 10th Anniversary Conf.* 101, March 11 1987. DOI: 10.1117/12.937536
- [24] Moeller RP et al. Open-loop output and scale-factor stability in a fiber-optic-gyroscope. *Journal of Lightwave Technology*. 1989;**7**(2):262-269
- [25] Ebberg A et al. Closed-loop fiber-optic gyroscope with a Sawtooth phase-modulated feedback. *Optics Letters*. 1985;**10**(6):300-302
- [26] Kay CJ et al. Serrodyne modulator in a fibre-optic gyroscope. *Optoelectronics, IEEE Proceedings Journal*. 1985;**132**(5):259-264
- [27] Yahalom R et al. Low-Cost, Compact Fiber-Optic Gyroscope For Super-Stable Line-Of-Sight Stabilization. *Proceedings of the IEEE/ION Position Location and Navigation Symposium (PLANS), Indian Wells, CA(USA)*. May 2010. DOI: 10.1109/PLANS.2010.5507131
- [28] Çelikel O et al. Establishment of all digital closed-loop Interferometric fiber-optic-gyroscope and scale factor comparison for open-loop and all digital closed-loop configurations. *IEEE Sensors Journal*. 2009;**9**(2):176-186
- [29] Sandoval-Romero GE et al. Límite de Detección de Un Giroscopio de Fibra Óptica Usando Una Fuente de Radiación Superluminiscente. *Rev. Mexicana de Física*. 2002; **49**(2):155-165
- [30] Medjadba H et al. Low-Cost Technique For Improving Open-Loop Fiber Optic Gyroscope Scale Factor Linearity. *Proceedings of the International Conference on Information and Communication Technologies, 2006 (ICTTA'06), 2, Damascus (Syria)*. 1684718, 2057–2060, April 24–28, 2006. DOI: 10.1109/ICTTA.2006
- [31] Bennett S et al. Fiber optic gyros for robotics. *Service Robot: An International Journal*. 1996;**2**(4)
- [32] Emge S et al. Reduced Minimum Configuration Fiber Optic Gyro for Land Navigation Applications. *Proc. SPIE 2837, Fiber Optic Gyros: 20th Anniversary Conf., Denver CO (USA)*, August 04, 1996
- [33] Bennett SM et al. Fiber optic gyroscopes for vehicular use. *Proceedings of the IEEE Conf. on Intelligent Transportation System (ITSC'97), Boston MA (USA)*, Nov. 9-12, 1997, 1053-1057. DOI: 10.1109/ITSC.1997.660619
- [34] Cordova A, Patterson R, Rahu J, Lam L, Rozelle D. Progress in navigation grade FOG performance. *SPIE Proceedings*. 1996;**2837**:2017-2217
- [35] Pavlath G. The LN200 fiber gyro based tactical grade IMU. *Proc. Guidance, Navigation and Control, AIAA*, pp. 898-904, 1993

- [36] Kamagai T et al. Fiber optic gyroscopes for vehicle navigation systems. *Fiber Optic Laser Sensors XI, Proceedings of SPIE*. Sept. 1993;**2070**:181-191
- [37] Hotate K, Tabe K. Drift of an optical fiber gyroscope caused by the faraday effect: Influence of the earth's magnetic field. *Applied Optics*. 1986;**25**:1086-1092
- [38] Bohm K, Petermann K, Weidel E. Sensitivity of a fiber optic gyroscope to environmental magnetic fields. *Optics Letters*. 1982;**6**:180-182
- [39] Blake JN. Magnetic field sensitivity of depolarized fiber optic gyros. *SPIE Proc.*, 1367, *Fiber Optic and Laser Sensors VIII*. pp. 81-86, 1990
- [40] Bergh RA, Lefevre HC, Shaw HJ. Compensation of the optical Kerr effect in fiber-optic gyroscopes. *Optics Letters*. June 1982;**7**:282-284
- [41] Takiguchi K, Hotate K. Method to reduce the optical Kerr-effect-induced bias in an optical passive ring-resonator gyro. *IEEE Photonics Technology Letters*. Feb. 1992;**4**:2
- [42] Bergh RA, Culshaw B, Cutler CC, Lefevre HC, Shaw HJ. Source statistics and the Kerr effect in fiber-optic gyroscopes. *Optics Letters*. 1982;**7**:563-565
- [43] Shupe DM. Thermally induced nonreciprocity in the fiber-optic interferometer. *Applied Optics*. 1980;**19**(5):654-665
- [44] Ruffin PB, Lofts CM, Sung CC, Page JL. Reduction of nonreciprocity in wound fiber optic interferometers. *Optical Engineering*. 1994;**33**(8):2675-2679
- [45] Lofts CM, Ruffin PB, Parker M, Sung CC. Investigation of effects of temporal thermal gradients in fiber optic gyroscope sensing coils. *Optical Engineering*. Oct. 1995;**34**(10):2853-2863
- [46] Sawyer J, Ruffin PB, Sung CC. Investigation of effects of temporal thermal gradients in fiber optic gyroscope sensing coils, part II. *Optical Engineering*. Jan. 1997;**36**(1):29-34
- [47] Ruffin PB, Sung CC, Morgan R. Analysis of temperature and stress effects in fiber optic gyroscopes. *Fiber Optic Gyros, Proceedings of SPIE*. Sept. 1991;**1585**:283-299
- [48] Frigo NJ. Compensation of linear sources of non-reciprocity in Sagnac interferometers. *Fiber Optic Laser Sensors I, SPIE Proceedings*. 1983;**412**:268-271
- [49] Ruffin PB, Baeder JS, Sung CC. Study of ultraminiature sensing coils and the performance of a depolarized interferometric fiber optic gyroscope. *Optical Engineering*. Apr. 2001;**40**(4):605-611
- [50] Lefevre HC, Bergh RA, Shaw HJ. All-fiber gyroscope with inertial navigation short-term sensitivity. *Optics Letters*. 1982;**7**:454-456

